small methods
www.small-methods.com

Comprehensive Osteosarcoma Treatment with Multifunctional Composite Hydrogels Enabling Combined Photothermal Cancer Ablation and Osteoinductive Tissue Regeneration

Hayeon Byun, Taeyeon Hwang, Hyoryong Lee, Yun-Jung Choi, Dong-Jae Kim, Eunji Park, Eunhyung Kim, Sukho Park, and Heungsoo Shin**

Osteosarcoma treatment can lead to considerable loss of bone tissue, creating a challenging microenvironment for recovery. Here, a novel biomaterial is described for tumor treatment via photothermal therapy and bone-tissue regeneration. Multifunctional composite hydrogels can be fabricated by incorporating mineralized magnetic fibers (G-mMFs) into a gelatin-genipin hydrogel. The G-mMFs exhibit notable temperature increases in response to near-infrared irradiation, and superior disruption of tumor tissue follows hyperthermia therapy in a tumor-bearing mouse model. G-mMFs protect stem cells from the oxidative stress anticipated after tumor ablation, following significant increases in catalase and anti-apoptotic gene expression. G-mMFs demonstrate enhanced osteoinductivity, with nearly 90% of human adipose-derived stem cells exhibiting osteogenic markers. Adenosine signaling–mediated osteogenesis and restoration of osteogenesis under oxidative stress can be demonstrated through stem-cell differentiation in the presence of H_2O_2. In vivo, regeneration of bone tissue can be assessed using a calvarial bone-defect mouse model, with nearly twice the amount of bone formation in the G-mMF group compared with mice without implantation, along with a more mature bone-tissue structure. Collectively, these study results present G-mMFs as a multifunctional biomaterial that simultaneously addresses tumor ablation and bone regeneration, offering a promising strategy for the comprehensive treatment of osteosarcoma.

1. Introduction

Osteosarcoma is a major malignant form of bone cancer, with event-free survival rates of less than 30% for metastatic patients.[1] While surgical removal has been the primary method of clinical treatment, the presence of residual cancer cells in adjacent bone tissue poses a significant risk of tumor recurrence or metastasis.[2] Commonly used treatments such as chemotherapy and radiotherapy involve severe pain and can lead to drug or radiation resistance, complicating tumor removal.[3] Such therapeutic applications are also associated with significant bone loss that can lead to chronic inflammation or, in severe instances, tissue necrosis during protracted tissue regeneration.[4] An extensive approach integrating tumor ablation and tissue regeneration is needed.

Photothermal therapy (PTT) is a promising non-invasive modality for tumor treatment due to its spatiotemporal

H. Byun, T. Hwang, E. Park, E. Kim, H. Shin
Department of Bioengineering
Hanyang University
222 Wangsimni-ro, Seongdong-gu, Seoul 04763, Republic of Korea
E-mail: hshin@hanyang.ac.kr

The ORCID identification number(s) for the author(s) of this article can be found under https://doi.org/10.1002/smtd.202500617

DOI: 10.1002/smtd.202500617

H. Lee, S. Park
Department of Robotics and Mechatronics Engineering
Daegu Gyeongbuk Institute of Science and Technology
333 Techno Jungang Daero, Hyeonpung-eup, Dalseong-gun, Daegu 42988, Republic of Korea
E-mail: shpark12@dgist.ac.kr

Y.-J. Choi, D.-J. Kim
Laboratory Animal Resource Center
Daegu Gyeongbuk Institute of Science and Technology
333 Techno Jungang Daero, Hyeonpung-eup, Dalseong-gun, Daegu 42988, Republic of Korea

H. Shin
Institute of Nano Science and Technology
Hanyang University
222 Wangsimni-ro, Seongdong-gu, Seoul 04763, Republic of Korea

selectivity and low toxicity.[5] Photothermal agents (PTAs), such as gold, carbon, and iron oxide nanomaterials, function as the principal heat sources in PTT by efficiently converting absorbed near-infrared (NIR) laser irradiation (800 to 1350 nm) into thermal energy.[6] Magnetic nanoparticles (MNPs) composed of Fe_3O_4 and characterized by robust NIR absorption, elevated photothermal-conversion efficiency, and excellent biocompatibility are appropriate materials for PTT.[7] Despite their advantages, the off-target effects of PTA can lead to undesirable side effects and diminished efficacy. While PTAs have been systematically administered, recent approaches using targeted delivery through antibody-mediated bioengineering techniques or hydrogels as delivery vehicles have been developed specifically to target tumors.[8]

Restoration of impaired tissue is an important aspect of treatment that many cancer-ablation techniques have neglected. Bone, a calcified tissue consisting of greater than 60% inorganic compounds, plays an indispensable role in protecting and supporting the body.[9] Because autogenous healing systems typically cannot fully regenerate severe bone defects, bone-tissue engineering with biomineral-based biomaterials such as hydroxyapatite and β-tricalcium phosphate is crucial.[9] Calcium phosphate (CaP)-based biomaterials occupy a unique position due to their chemical resemblance to the constituents and architecture of natural bone tissue.[10] Biomaterials mimicking the mineral environment of bone tissue exert a significant influence on cell behavior and the bone healing process, both mechanically and biophysically.[11] Metal ions, such as Ca^{2+} and Sr^{2+}, promote osteogenic differentiation of stem and progenitor cells, facilitating the formation of bone tissue.[12] PO_4^{3-} and Ca^{2+} participate in osteogenesis and angiogenesis through adenosine-mediated signaling in the A2B receptor pathway.[13] This allows a significant potential of fibrous mineralized materials to replicate the biomineralization process that transpires along collagen fibrils, using the biophysical properties of these biomineral substances.[14]

Reactive oxygen species (ROS), which can impede wound healing, are produced through various factors such as infection, cell death, or metabolic activity, alongside tumor ablation and tissue regeneration.[15] In bone-tissue regeneration, excessive generation of ROS hinders osteoblast function and postpones bone formation,[16,17] and numerous strategies have been devised to regulate ROS post-injury.[18] Naturally sourced polyphenols, such as epigallocatechin gallate (EGCG), curcumin, and tannic acid, can be used to modulate ROS levels in a biocompatible fashion.[19] A polyphenol that has been evaluated by the U.S. Food and Drug Administration, EGCG has a significant ability to scavenge ROS and exhibits superior biocompatibility.[20] EGCG can also advance the engineering of biomaterials due to its chemical properties, including oxidative polymerization and metal-phenol networks (MPNs), which can augment the biological activities of biomaterials.[21] For example, polycaprolactone film coated with EGCG exhibited a notable radical scavenging efficacy of ≈60%.[22] Despite the widespread application of EGCG for surface functionalization in previous studies, little research has been conducted on mineralization utilizing EGCG.[23] Furthermore, given that EGCG influences cancer progression via laminin receptors, it represents a promising candidate for cancer therapy and tissue regeneration.[24]

In this study, we developed composite hydrogels incorporating multifunctional mineralized magnetic nanofibers (mMFs) to address osteosarcoma treatment and simultaneously accelerate the regeneration of bone tissue (**Figure 1**). While composite hydrogels have been widely investigated for therapeutic use, integrated strategies that simultaneously achieve tumor ablation and tissue regeneration via sustained release of bioactive molecules remain limited. MNPs encapsulated within the nanofibers exhibited a notable exothermic ability under NIR irradiation, even after being embedded into a genipin-gelatin (gelapin) hydrogel. After NIR irradiation, the temperature of hydrogels increased to 45°C, inducing tumor cell death, in both in vitro MG63 osteosarcoma cells and a xenograft mouse in vivo model. In addition, hydrogels with mMFs showed great potential in ROS regulation as well as osteogenic differentiation of human adipose-derived stem cells (hADSCs). mMF hydrogels protect cells from apoptosis under severe ROS conditions through both ROS scavenging and induction of catalase production. They also enhance calcium deposition and osteogenic marker expression through adenosine signaling of hADSCs, even under ROS stress. Evaluation of bone-tissue regeneration using an in vivo calvarial-defect mouse model demonstrates the potent bone growth effect of mMF hydrogels. Collectively, we anticipate that this novel approach, which addresses both tumor ablation and bone-tissue regeneration, will provide a new perspective on cancer treatment.

2. Results and Discussion

2.1. Fabrication and Characterization of mMFs

A transmission electron microscope (TEM) image of an mMF revealed internalized MNPs along a poly-L-lactic acid (PLLA) nanofiber (**Figure 2a**). Scanning electron microscope (SEM) images of mMFs showed a uniform, flake-like mineral coating ≈200 µm thick (Figure 2b; Figure S1, Supporting Information). Because micro-scaled nanofibers can replicate the natural structure of the extracellular matrix,[25] we chose MNP-embedded PLLA nanofibers for photothermal therapy, based on previous reports indicating that MNPs within synthetic polymers retain their responsiveness to external stimuli.[26–28] We also sought to enhance functionality through surface modification of nanofibers with minerals and polyphenols. Fourier-transform infrared (FTIR) analysis revealed extensive and broad O—H stretching in the mMF group between 3200 and 3700 cm^{-1}, indicating deposition of EGCG on the fiber surface.[29] The PO_4^{3-} peak at 556 cm^{-1} was exclusively observed in mMFs, signifying CaP-based mineralization. Conversely, the peaks corresponding to C═O (1718 cm^{-1})[30] and CH_3 bending (1300 and 1400 cm^{-1}), prevalent in PLLA monomers,[31] diminished following mineralization (Figure 2c). In accordance with the FTIR analysis, a reduction in the C═O and C—O peaks was observed in the C 1s peak in X-ray photoelectron spectroscopy (XPS) analysis (Figure 2d). In addition, distinct Ca 2p and P 2p peaks were detected in the mMF, whereas the Fe 2p peak vanished after mineralization, indicating the encasement of MNPs within the fiber by a substantial mineral layer.

Mineralization of fibers based on an MPN has significant potential in bone tissue engineering due to their osteoinductivity, superior mechanical properties, and structural similarity to

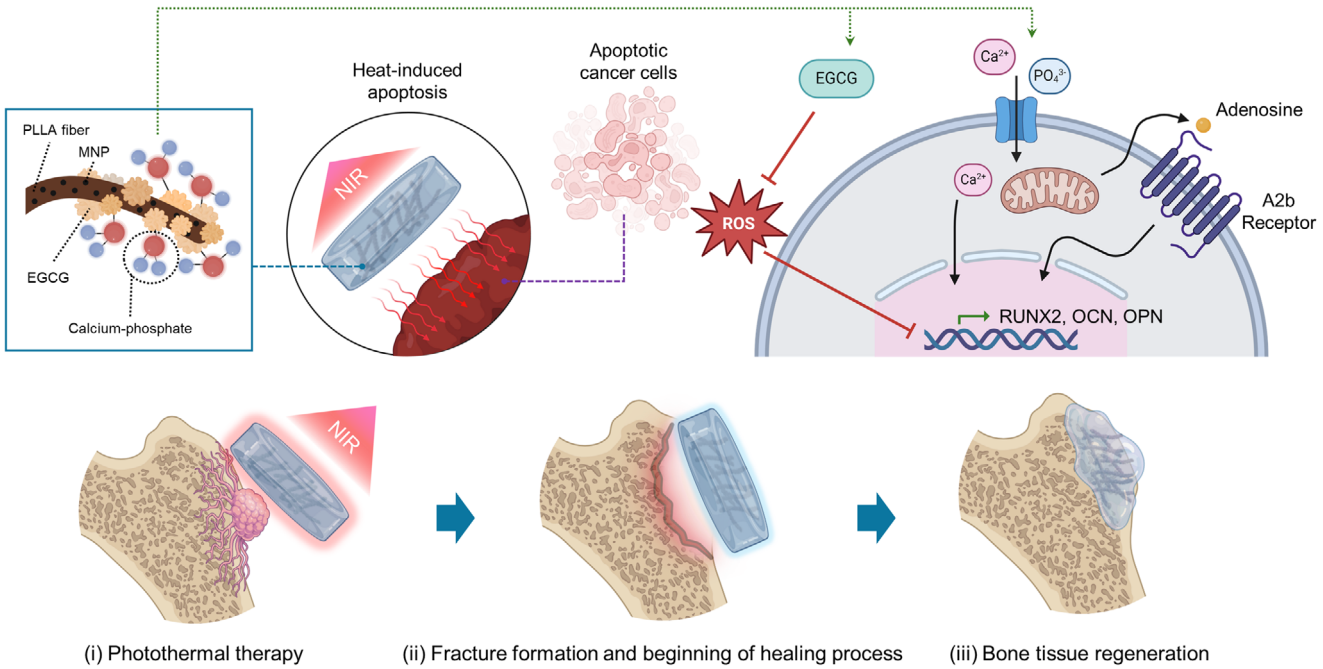

Figure 1. The synthesis of multifunctional composite hydrogels, subsequently integrated cancer treatment, and bone-tissue regeneration are depicted schematically. Mineralized magnetic fibers (mMFs) were synthesized using an epigallocatechin gallate (EGCG) and mineral coating on magnetic nanoparticle (MNP)-dispersed synthetic nanofibers. Upon incorporation into the gelapin hydrogel, heat-induced apoptosis was triggered in the tumor cells following near-infrared (NIR) irradiation of the hydrogels. Subsequently, the hydrogels began promoting the healing process by EGCG-mediated scavenging of reactive oxygen species (ROS) released by damaged and dying cells. Meanwhile, calcium phosphate–based minerals stimulated osteogenesis in stem cells through adenosine signaling by enhancing the expression of osteogenic marker genes such as *RUNX2*, *OCN*, and *OPN*, leading to regeneration of bone tissue analogous to normal tissue.

mineralized bone extracellular matrix, rendering them ideal biomaterials for this application.[14,30] This method also has a significant potential to harness the biological functions of both minerals and polyphenols.[32] In this study, we used an MPN-based rapid mineralization technique by altering the composition of 10× simulated body fluid (SBF) to maximize CaP deposition.[33] Consequently, nearly 200 µg of calcium was deposited onto 1 mg of fibers (Figure 2e). The quantity of EGCG produced was 180 µg per 1 mg of fibers (Figure 2f). The mMFs exhibited dose-dependent radical scavenging abilities of EGCG, as shown by a Fe conversion rate of ≈50% and mineral deposition (Figure 2g). We were able to control the length of nanofibers from 10 to 100 µm, and the fibers were successfully coated with minerals irrespective of their length (Figure S1, Supporting Information). Collectively, these results demonstrate the precise engineering of mineralized fibers of varying dimensions and functionalization.

2.2. Characterization of G-mMFs

We synthesized composite hydrogels using multifunctional mMFs and gelapin via cryogelation (**Figure 3a**). We used genipin as a crosslinker as it is more biocompatible than other chemical crosslinkers such as glutaraldehyde.[34] Although genipin-based hydrogels are widely used in biomedical applications, genipin as a crosslinker provides limited biological functionality. To address this, we reinforced the hydrogel by incorporating additional multifunctional biomaterials to enhance its therapeutic potential. Embedding mineral-coated fibers into the biodegradable hydrogel matrix not only imparts biological functionality but also improves the hydrogel's spatiotemporal stability, making it a promising strategy for tissue engineering applications.[35] For example, Kashimura et al. reported augmenting the mechanical strength of poly(acrylic acid) hydrogels by integrating hydroxyapatite nanoparticles.[36] Consistent with this, SEM images revealed comparable surface morphologies across groups, while the pore size and swelling ratio of the hydrogels after drying decreased with an increase in mMF quantity (Figure 3b; Figure S2, Supporting Information). Conversely, the storage modulus was enhanced with further addition of mMFs to the hydrogels (Figure 3c), likely due to the formation of a denser polymer network incorporating mineral-coated fibers.[37] In addition, fibrous Mineral-deposited fibers were also observed after hydrogel encapsulation by energy-dispersive X-ray spectroscopy (EDS) mapping (Figure 3d). A fibrous morphology was retained within the hydrogel, indicating the distribution of mMFs along the hydrogel backbone (Figure 3e). The concentrations of calcium and EGCG in the hydrogels increased with the mMF concentration (Figure S3, Supporting Information). Hydrogels containing mMFs retarded the degradation (Figure 3f), indicating that mMFs reinforced the hydrogels to withstand hydrolysis of the gelatin backbone.[38] All hydrogels, despite variations in degradation rates, were completely degraded after 4 h of incubation with 1.0 CDU mL^{-1} of collagenase (Figure 3g). Since this material possesses photothermal properties, we additionally evaluated the stability of the hydrogel under NIR irradiation. For all hydrogels

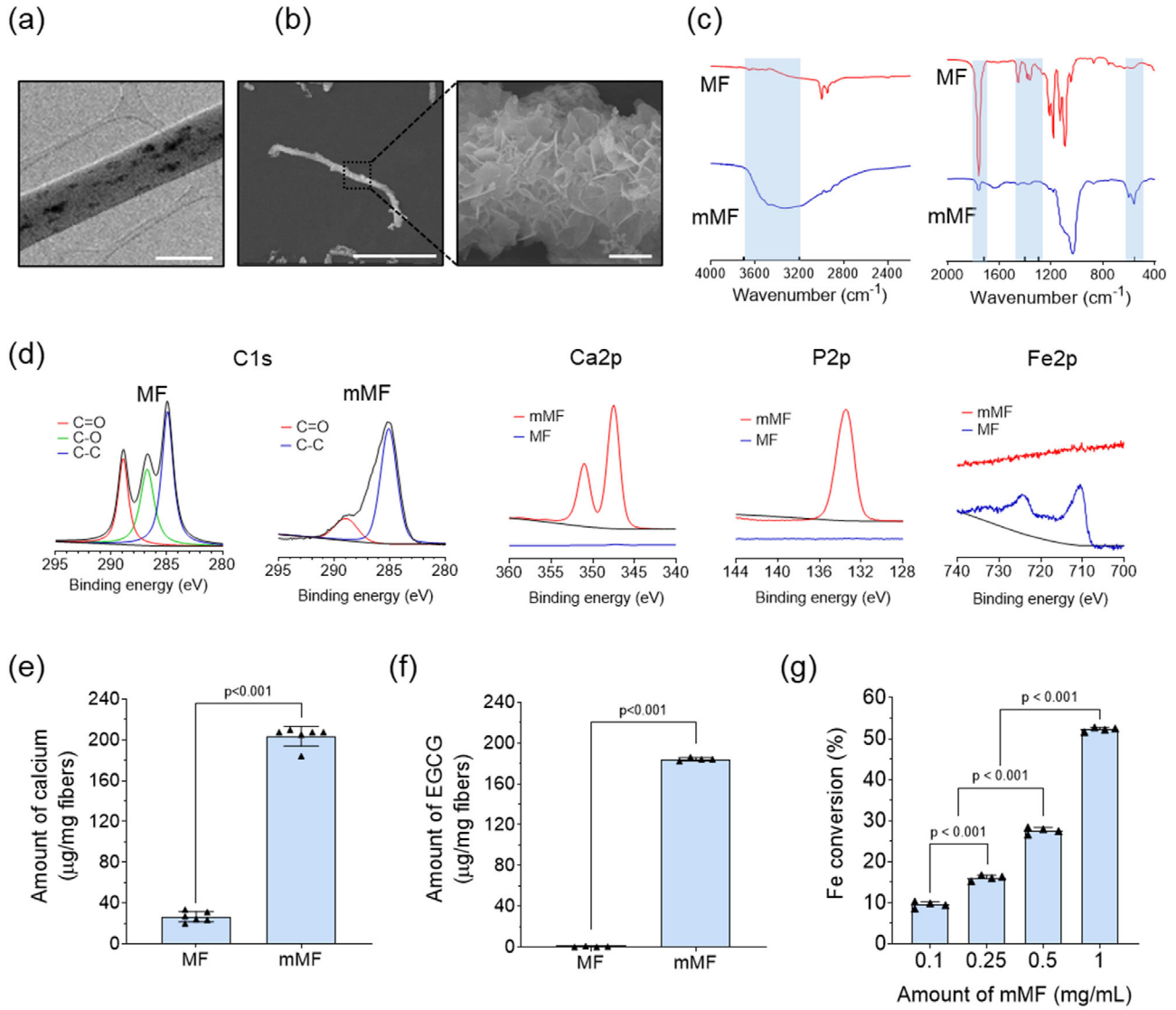

Figure 2. Characterization of mMFs. a) Transmission electron microscopy (TEM) image of magnetic fibers. Scale bar = 500 nm. b) Scanning electron microscopy (SEM) images of the mMF. Scale bar = 50 μm (left), 1 μm (right). c) FTIR analysis of the MF and mMF. d) High-resolution XPS results for the C 1s, Ca 2p, Fe 2p, and P 2p peaks of the MF and mMF. The amounts of e) calcium ($n = 6$) and f) EGCG on the fibers ($n = 4$). g) Fe conversion results of mMFs at varying concentrations ($n = 4$).

containing biomineral components, the release of EGCG and calcium reached a maximum of ≈35% and 13%, respectively, after 72 h and then showed a tendency of saturation (Figure S4, Supporting Information). Enhanced Fe conversion rates exhibited the sustained radical-scavenging ability of EGCG on the mMFs, even after incorporation into hydrogels (Figure 3h). Hydrogels without mMFs achieved a Fe conversion rate of ≈20% due to the radical-scavenging effect of the genipin-based hydrogel.[39] The biocompatibility of the G-mMFs was assessed using live/dead staining. After 24 h of incubation, the hydrogels showed no detrimental effect on the viability of hADSCs (Figure 3i). The DNA assay results corroborated the cytocompatibility of the hydrogels by demonstrating identical DNA content on day 1 between groups (Figure 3j). However, the DNA content was lower in the hydrogels containing mMFs on day 7 compared to those without, and we anticipate that this delayed proliferation from the differentiation of the stem cells,[40] as discussed in section 2.5.

2.3. Photothermal Tumor Ablation Using G-mMF

As the amount of mMF increased, the temperature of the hydrogels exposed to NIR irradiation for 3 min increased from 38.3 °C (0 mg mL^{-1}) to 44.8 °C (8 mg mL^{-1}) in phosphate-buffered saline (PBS) (**Figure** 4a). Temperature variations persisted during five iterations of NIR irradiation, indicating the potential for repeated photothermal therapy application. The MG63 cells grown on the hydrogels containing the mMFs exhibited noticeably fewer viable cells following NIR irradiation (Figure 4b). Even in the absence of NIR irradiation, the DNA content of the MG63 cells grown

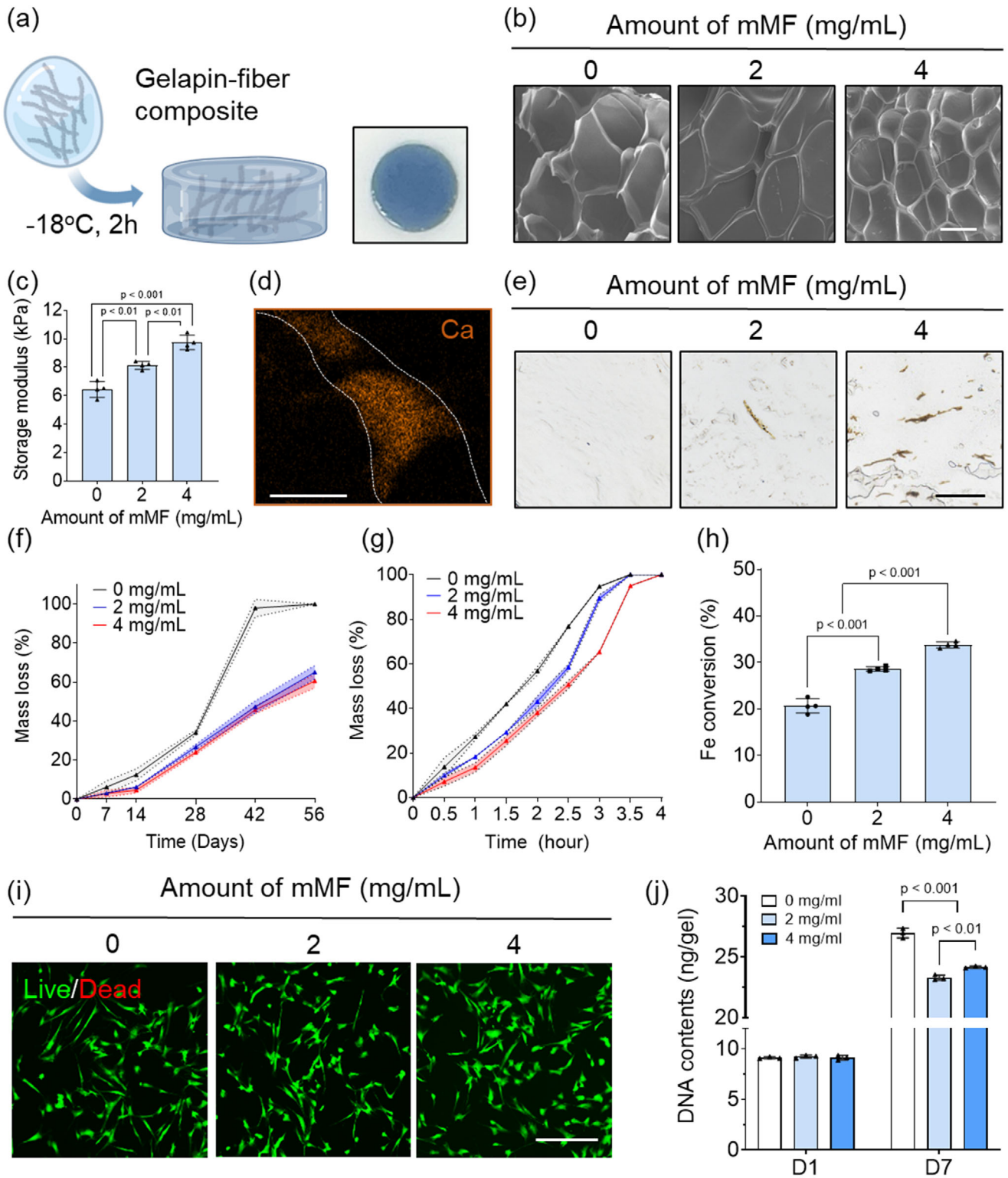

Figure 3. Characterization of G-mMFs. a) Schematic of gelapin-mMF hydrogel (G-mMF) fabrication. The gelapin solution dispersed with mMFs was stored at −18°C for 2 h to facilitate crosslinking. The hydrogels were punched in various sizes for specific experiments, as depicted in the optical image. b) SEM images of G-mMFs at varying mMF concentrations. Scale bar = 100 µm. c) Storage modulus of hydrogels containing varying quantities of mMFs ($n = 4$). d) EDS mapping image of mMF for a calcium channel. Scale bar = 5 µm. e) Optical images of G-mMF stained using von Kossa staining. Scale bar = 200 µm. The degradation kinetics of hydrogels under f) non-enzymatic and g) enzymatic environments ($n = 5$). h) Fe conversion results of G-mMFs ($n = 4$). i) Fluorescent images of human adipose-derived stem cells (hADSCs) from live/dead staining following 24 h of culturing on G-mMFs. Scale bar = 200 µm. j) DNA content in the G-mMFs after culturing for 1 and 7 days with hADSCs ($n = 3$).

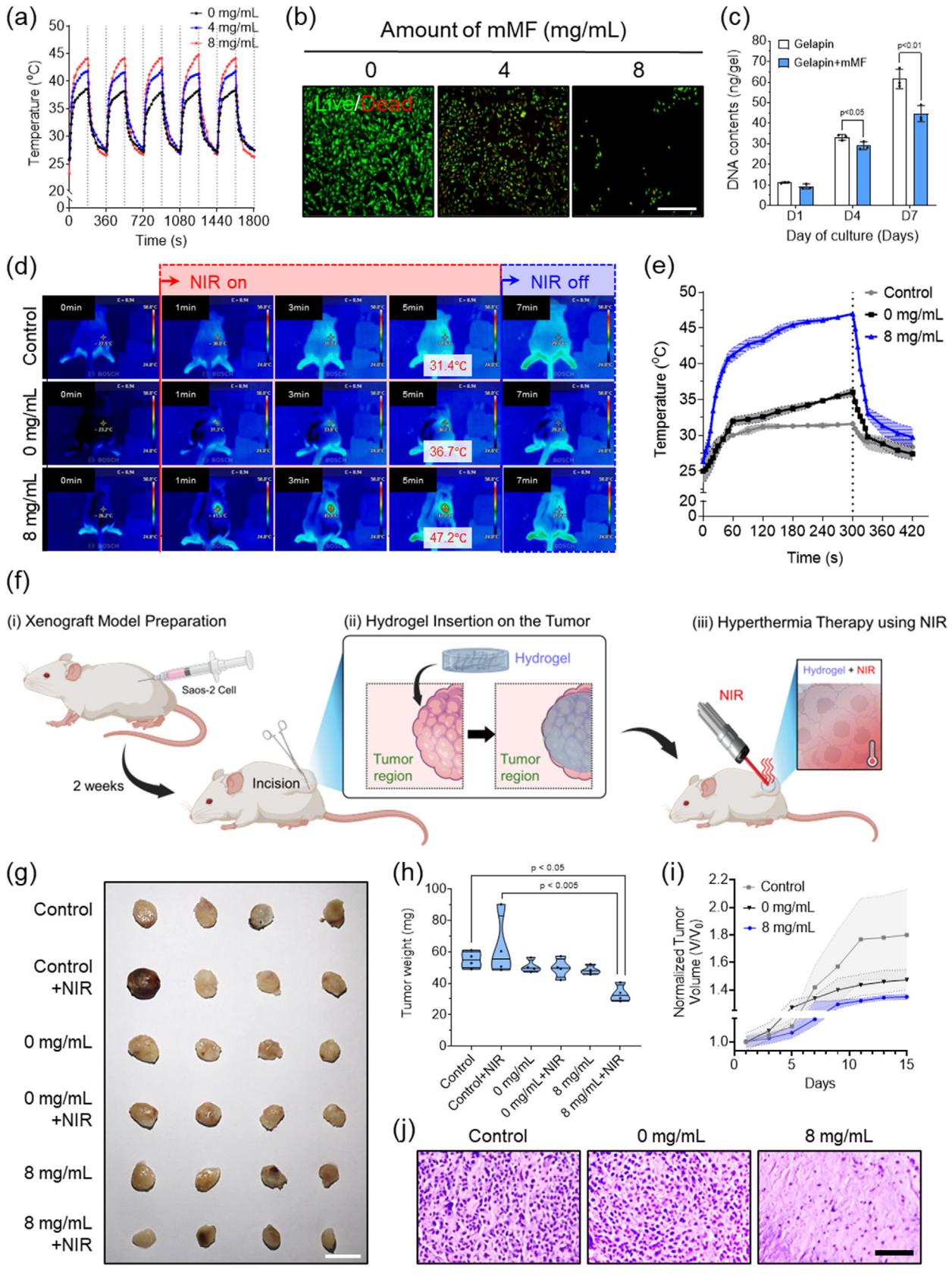

on the G-mMF (4 mg mL^{-1}) was substantially lower than that of cells grown on the hydrogel without mMF (Figure 4c). EGCG reportedly exerts an anticancer effect by acting downstream of laminin receptor signaling.[24] As a result, released EGCG appeared to control the growth of MG63 cells, which is desirable to regulate remaining cancer cells to prevent tumor recurrence.[41] Hydrogels containing 8 mg mL^{-1} of mMFs demonstrated a temperature increase to 47.2°C after implantation into subcutaneous areas of the mice, which is thought to be sufficient to cause heat-activated apoptosis of tumor cells (Figure 4d,e).[42] Prior to the subsequent treatment, the temperature decreased to its normal level, indicating recovery of the tissue microenvironment.

Figure 4f is a schematic of the creation of a xenograft osteosarcoma model and hyperthermia therapy. In summary, hydrogels containing Saos-2 cells were administered subcutaneously into mice and allowed to develop for two weeks. Through a tiny incision on the mouse skin, hydrogels were applied to the tumor, which was then exposed to NIR radiation to induce hyperthermia. Compared with the other groups, the removed tumors incubated with G-mMFs were smaller and 8 mg mL^{-1} G-mMF with NIR showed significantly reduced size compared to others (Figure 4g; Figure S5, Supporting Information). However, compared with control groups, the tumor weight was significantly lower only in the 8 mg mL^{-1} mMF group exposed to NIR irradiation (Figure 4h). The growth of tumors was inhibited by heat, as shown by the normalized tumor volume during treatment (Figure 4i). The results of a histological investigation revealed scant hematoxylin staining in the G-mMF group, indicating that the tissue had collapsed as a result of cancer cell death (Figure 4j). Long-term exposure to heat greater than 47 °C caused cancer cells to undergo apoptosis in heat-induced cancer therapy.[42] TUNEL staining demonstrated significant apoptosis in the 8 mg mL^{-1} group following NIR irradiation (Figure S6, Supporting Information). However, prolonged heat exposure during photothermal therapy can cause severe damage not only to cancer cells but also to surrounding normal tissues. Such tissue damage is often associated with excessive accumulation of ROS, leading to fibrosis and permanent tissue scarring.[43] The substantial retention of ECM, as observed in Figure 4j, further supports this concern. Therefore, a more comprehensive strategy that integrates tissue engineering approaches is required to facilitate proper tissue remodeling and recovery following treatment.

2.4. ROS-Scavenging Properties of G-mMF

After tumor therapy, elevated levels of ROS may arise from cellular apoptosis, alongside increased inflammation due to elevated temperatures, which can attract activated immune cells including macrophages and neutrophils.[44] Elevated metabolic activity produces excessive ROS, which can lead to cell death and impede tissue regeneration.[45] A strategy for engineering biomaterials to modulate ROS produced during tumor ablation is needed. We hypothesized that EGCG integrated into mMFs will have significant ROS-scavenging ability, and we observed decreased cytotoxicity after the application of H_2O_2, a major ROS. A reduction in H_2O_2 levels was evident with increasing quantity of mMFs during incubation with varying concentrations of fibers and hydrogels containing different mMFs (Figure S7, Supporting Information). The ROS scavenging capacity of biomaterials can be influenced by various soluble compounds present in physiological environments, including amino acids and phenolic molecules.[46] To ensure a more systematic and physiologically relevant evaluation, the ROS scavenging ability of G-mMFs was assessed under conditions where ROS were introduced in the culture medium. The live/dead staining results illustrated enhanced viability of hADSCs cultured on hydrogels containing a larger number of mMFs when subjected to 1000 μM H_2O_2, which is an extreme ROS condition (**Figure 5a**). Conversely, dead signals were decreased by elevated mMF concentrations. Trends revealed by TUNEL staining were analogous to those of dead-cell staining. Furthermore, significant differences in viability were evident between the groups under treatment with both 500 and 1000 μM H_2O_2. Only 20 to 30% of cells survived on hydrogel under these two conditions, whereas ≈70% of the cells remained viable on hydrogel containing 4 mg mL^{-1} mMF (Figure 5b). The number of TUNEL-positive signals in the 4 mg mL^{-1} group was approximately one-fourth that in the 0 mg mL^{-1} group (Figure 5c).

While polyphenols can directly scavenge ROS, they also regulate ROS via intracellular signaling pathways.[47] EGCG reportedly stimulates the expression of the *CAT* gene through the NRF2 signaling pathway, resulting in increased secretion of catalase to safeguard cells from H_2O_2-induced oxidative stress.[48] The expression of *CAT* in cells cultured on the G-mMF was 20 times that of the control group (0 mg mL^{-1}) (Figure 5d). Consequently, the expression of genes associated with the anti-apoptotic pathway, including *BCL-XL*, was elevated by the quantity of mMFs (Figure 5e). Conversely, genes associated with apoptosis, including *BAX*, *CAS3*, and *CAS9*, were markedly reduced in the presence of mMFs (Figure 5f). We anticipated that EGCG immobilized on mMFs can protect stem cells by neutralizing the surplus ROS produced during tumor therapy through both intra- and extracellular mechanisms.

2.5. Effect of G-mMF on Osteogenic Differentiation of Stem Cells

Expression of OPN and OCN proteins in hADSCs cultured on the hydrogels was augmented by the quantity of mMF in the hydrogels (**Figure 6a**). Cells with positive signals for both OPN and OCN represented almost 90% of the 4 mg mL^{-1} group

Figure 4. The photothermal effect of G-mMFs under near-infrared irradiation and in vivo tumor ablation. a) Temperature variations of the hydrogels during repeated NIR laser irradiation. b) Live/dead staining images of MG63 cells on the G-mMF subjected to NIR irradiation for 24 h. Scale bar = 200 μm. c) DNA contents of the MG63 cells cultured on hydrogels without NIR irradiation ($n = 3$). d) Time-course infrared thermal images of a mouse dermis after hydrogel implantation. e) Temperature variations in the mouse dermis with hydrogel implantation under NIR irradiation ($n = 3$). f) Schematic of the procedure for creating a tumor-bearing mouse model and administering hypothermal therapy using composite hydrogels and a NIR laser. Saos-2 cells were implanted subcutaneously in the mice, and tumors were allowed to develop for two weeks. Hydrogels were applied to the tumor area through an incision, and NIR induced hyperthermal therapy for 15 days. g) Optical images and h) tumor weights from tumor-bearing mice following 15 days of treatment ($n = 4$). Scale bar = 1 cm. i) Volume of tumors normalized by the weight of the mouse during treatment. (V: tumor volume at each time point, V0: initial tumor volume) ($n = 4$). j) H&E staining images of residual tumor following 15 days of treatment. Scale bar = 100 μm.

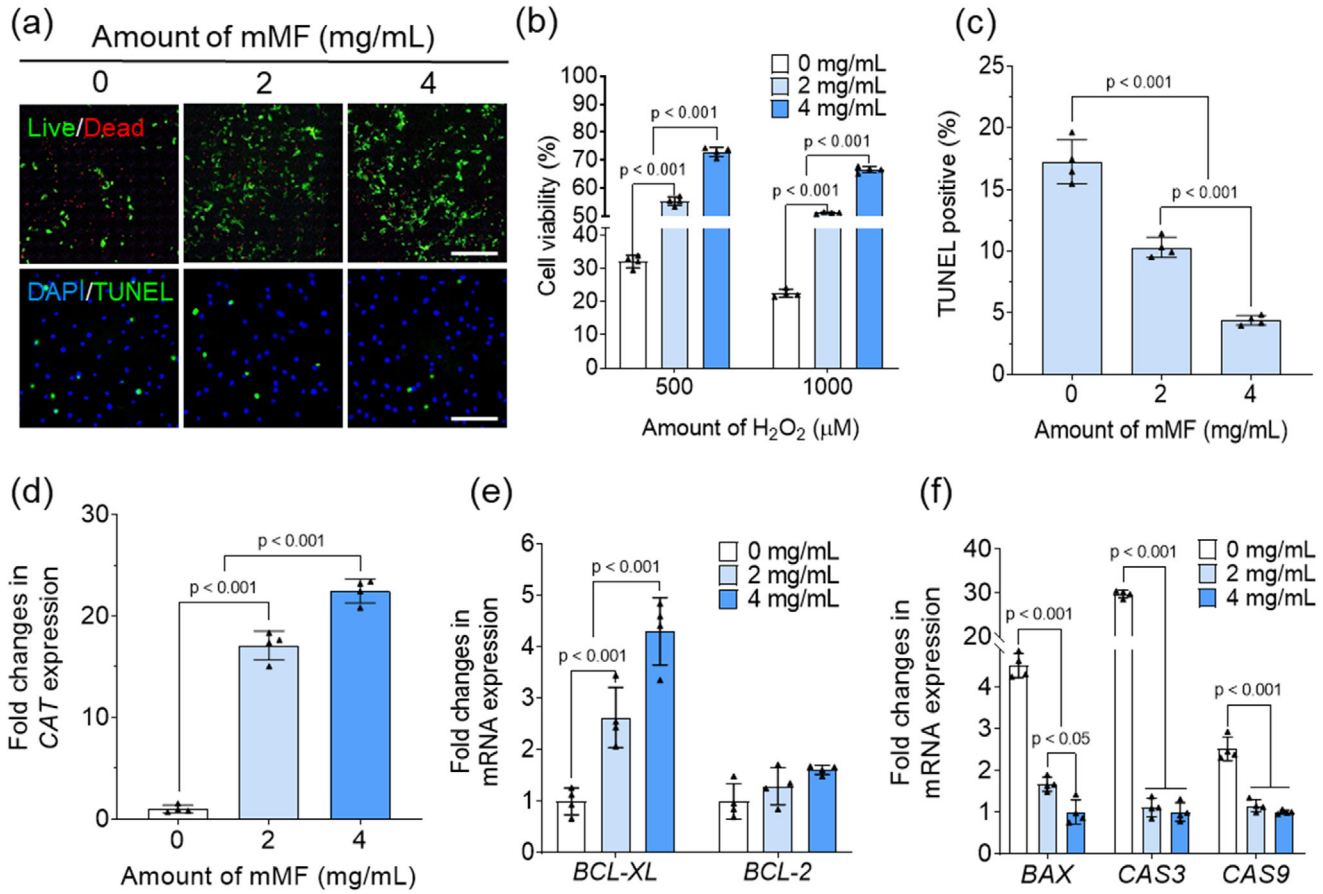

Figure 5. ROS scavenging properties of G-mMFs. a) Images from live/dead and TUNEL assays of hADSCs cultured on hydrogels with 1000 μM of H_2O_2 for 24 h. Scale bar = 200 μm. b) Viability of hADSCs cultured on hydrogels with 500 or 1000 μM of H_2O_2 for 24 h ($n = 4$). c) TUNEL-positive cells were quantified using the TUNEL assay. TUNEL positivity rate = (TUNEL positive signal / DAPI count) × 100 (%) ($n = 4$). Relative gene expression of hADSCs cultured with 500 μM of H_2O_2 for 24 h for d) *CAT*, e) anti-apoptotic genes (*BCL-XL*, *BCL-2*) and f) pro-apoptotic genes (*BAX*, *CAS3*, *CAS9*) ($n = 4$).

(Figure S8a, Supporting Information). The alkaline phosphatase content of the hADSCs, normalized to DNA content, was nearly twice as high in the 4 mg mL^{-1} group compared with the 0 mg mL^{-1} group (Figure 6b). The increase in calcium levels of cells from day 1 to day 14 was significantly greater in the 4 mg mL^{-1} group, indicating cell calcification through osteogenesis (Figure 6c). Calcium deposition was also observed through Alizarin red S staining, which revealed dense staining in cells cultured on mMF-containing hydrogels (Figure 6d). Mineralized biomaterials typically promote osteogenesis by releasing ions, including calcium and phosphate.[13] MPN-based minerals exhibited direct osteoinductivity in contrast to traditional mineralized biomaterials such as hydroxyapatite, which can be attributed to an amorphous feature that facilitates ion release.[21,33] The mMFs effectively differentiated the stem cells through sustained release of EGCG and calcium. We also expected that a substantial increase in calcium deposition would enhance bone-tissue regeneration by mineralizing the extracellular matrix surrounding newly formed bone tissue.[11]

The osteoinductivity of G-mMFs was assessed by examining adenosine signaling mechanisms with an A2B receptor agonist. The expression of *OPN* and *OCN* in hADSCs cultured on hydrogels increased with the quantity of mMF in the absence of PSB 603 treatment (Figure 6e). However, gene expression was downregulated in all groups to that of the control group (0 mg mL^{-1}) following treatment with PSB 603. Other osteogenic markers, such as *RUNX2* and *OSX*, exhibited similar trends (Figure S8b, Supporting Information). Calcium phosphates are the primary inorganic components, accounting for more than 60% of bone tissue.[49] Mineral-based biomaterials, including hydroxyapatite and whitlockite, have been used to promote osteogenesis by facilitating calcium and phosphate signaling, which activates calcium-channel and adenosine signaling pathways.[10] Increased levels of PO_4^{3-} can enhance ATP synthesis, resulting in the production of adenosine. This adenosine binds to the A2b receptor, facilitating osteogenic differentiation in stem cells.[13] Our findings indicate that mMFs promote the osteogenesis of hADSCs via adenosine signaling through this mechanism. During osteogenesis, ROS reportedly inhibits the Wnt signaling pathway, which is critical for osteogenic differentiation.[50,51] The presence of H_2O_2 resulted in a decrease in the expression of osteogenic genes (*OPN*, *OCN*, *RUNX2*, and *OSX*) in hADSCs; however, mMF-containing hydrogels restored expression (Figure 6f; Figure S5c, Supporting Information). In specific scenarios, such as post-cancer therapy, where there is substantial production of ROS, the conditions for bone regeneration are anticipated to be more challenging.[17]

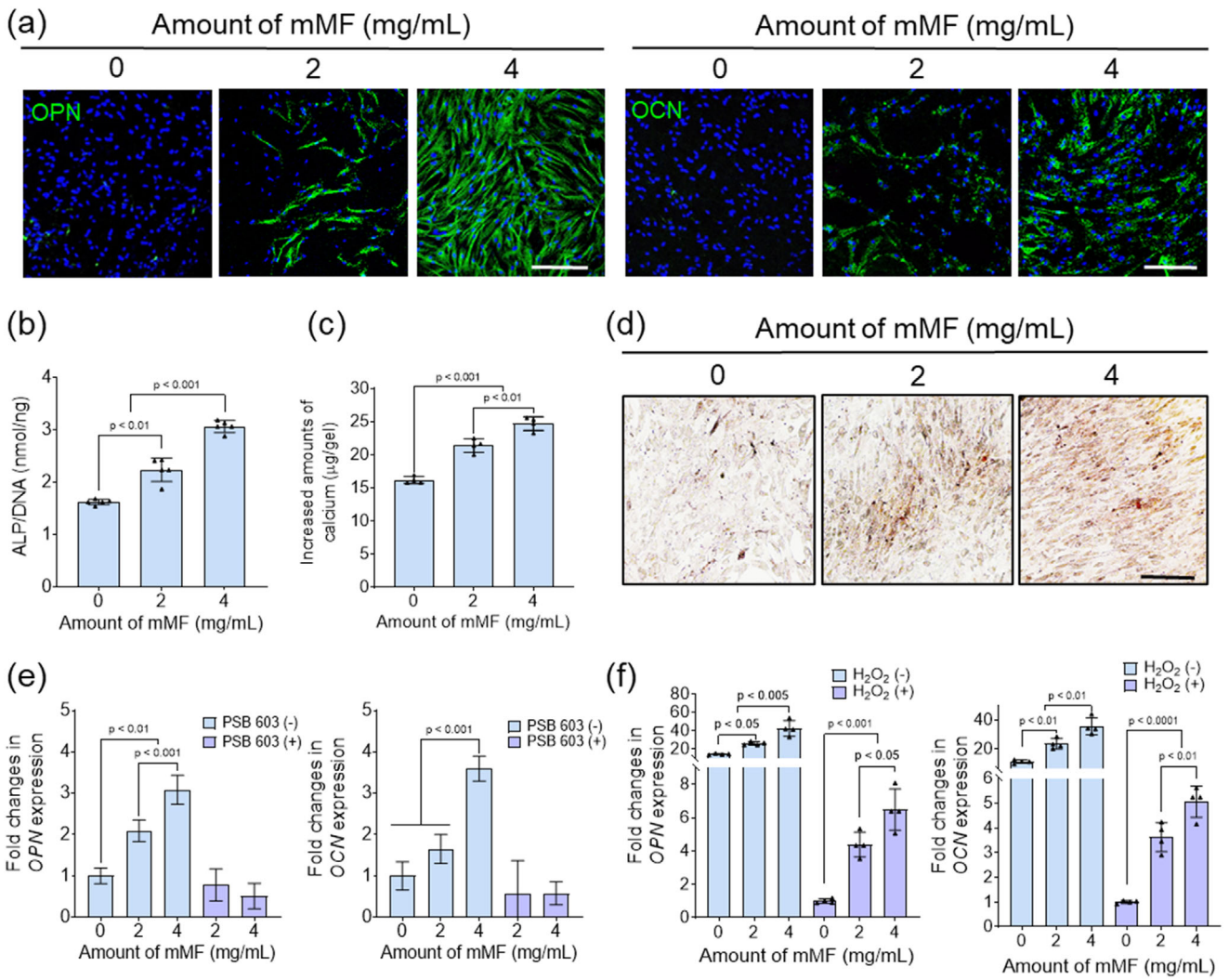

Figure 6. Effect of G-mMFs on osteogenic differentiation of hADSCs. a) Immunostaining images of hADSCs specific to OPN and OCN. Scale bar = 200 μm. b) Results of the alkaline phosphatase (ALP) assay for hADSCs cultured on hydrogels for 7 days, normalized to DNA content ($n = 5$). c) Increasing calcium levels in hADSCs cultured on G-mMF for 14 days ($n = 3$). d) Images of Alizarin red S staining of hADSCs cultured with varying quantities of mMFs for 14 days. Scale bar = 200 μm. Relative mRNA expression of osteogenic markers for e) *OPN* and *OCN* in hADSCs cultured with different quantities of G-mMFs, with or without PSB 603, over a period of 14 days ($n = 3$). Relative mRNA expression of the osteogenic markers f) *OPN* and *OCN* in hADSCs cultured on G-mMFs, with or without 200 μM of H_2O_2 for 14 days ($n = 4$).

In this context, mMF is expected to offer significant benefits through ROS regulation and osteoinductivity.

2.6. In Vivo Bone-Tissue Regeneration Using G-mMF

Bone-tissue formation in a complex in vivo microenvironment was evaluated using a mouse calvarial-bone-defect model. Conventional treatment of osteosarcoma frequently results in substantial bone loss, and this critical bone-defect model is a suitable representation of post-treatment conditions.[1] Microcomputed tomography images revealed a marked increase in the formation of bone tissue in the presence of mMFs relative to conditions without mMFs (**Figure** 7a). Quantitative analysis indicated that the area of the regenerated bone was ≈1.5 times larger in the presence of mMF (Figure 7b). Additionally, the volume of bone regenerated in the 8 mg mL^{-1} group was more than twice that of the defect group and was the most substantial increase in bone volume observed (Figure 7c).

The results of hematoxylin and eosin (H&E) staining demonstrated that an increase in mMF number resulted in thicker regenerated tissue with denser bone and more mature structures (Figure 7d). In addition, the implanted hydrogels were confirmed to have completely degraded over the 8-week healing period, indicating significant biodegradability of the biomaterials. Goldner's trichrome staining of the bone extracellular matrix revealed significantly darker collagen signals in the mMF-containing groups, indicating that these more mature bone tissues may facilitate the development of more complete bone tissue, even in the absence of degraded biomaterials (Figure 7e; Figure S9, Supporting Information). Immunofluorescent images of OCN expression revealed increasingly distinct signals with higher mMF content

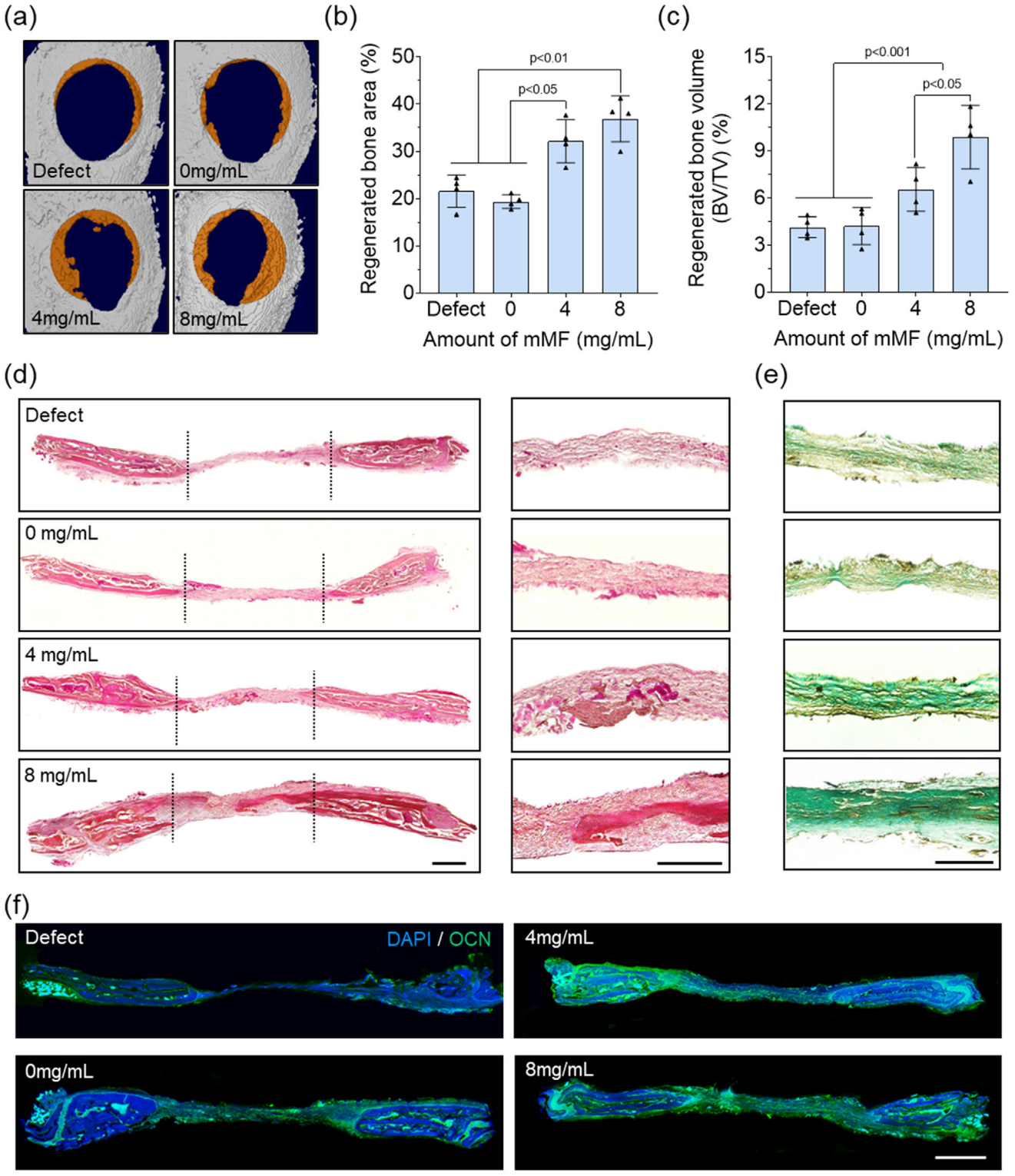

Figure 7. Effect of G-mMFs on in vivo bone-tissue regeneration. a) Micro-CT analysis and quantification of regenerated bone b) area and c) volume of calvarial defects eight weeks post G-mMF implantation ($n = 4$). Histological examination of regenerated bone through d) H&E staining and e) Goldner's trichrome staining. Scale bar = 1 mm (left) and 500 µm (right). f) Immunofluorescent staining for OCN was conducted eight weeks post-implantation. Scale bar = 250 µm.

(Figure 7f; Figure S9c, Supporting Information). OCN is essential for calcium deposition in bone-tissue regeneration, and the high expression of OCN in defect regions indicates the potential for enhanced mineralized bone tissue formation.[52] Furthermore, earlier markers such as RUNX2 and OPN were predominantly detected in the 4 and 8 mg mL^{-1} groups, suggesting that recruitment or differentiation of stem cells or osteoblasts may enhance regeneration of bone tissue (Figure S10, Supporting Information).[53] Interestingly, while OCN was broadly detected throughout the calcified regions, indicating overall progression of calcification, early stem cell differentiation markers such as RUNX and OPN were predominantly expressed in the peripheral areas. This spatial distribution suggests the potential of the hydrogel to support guided regeneration. These findings underscore the osteogenic potential of G-mMF in an in vivo model, indicating that G-mMF can promote rapid and mature recovery of critical defects due to osteosarcoma treatment.

In summary, our method offers marked improvements over conventional approaches. Employing inorganic osteoinductive factors with superior thermostability compared with organic growth factors, we successfully induced osteogenesis following thermotherapy. The use of hydrogel-based phototherapy effectively mitigated the off-target delivery issues commonly associated with systemic nanoparticle administration. At this stage, our study still has room for improvement in achieving faster tissue regeneration and enhanced anti-cancer efficacy. These outcomes may potentially be realized through the co-delivery of growth factors or anti-cancer drugs. Furthermore, aspects not explored in this study such as material-induced pathological responses and immunomodulatory effects remain important topics for future investigation. Nevertheless, the present findings underscore the potential of our proof-of-concept strategy. We anticipate that forthcoming innovations, such as the development of thermostable and potent osteoinductive molecules, will further strengthen this approach, ultimately enabling a more robust dual therapy for tumor ablation and tissue regeneration.

3. Conclusion

We developed a multifunctional composite hydrogel for photothermal therapy of osteosarcoma and subsequent bone tissue regeneration. The mMFs were synthesized via a one-step mineralization process using a modified 10× SBF solution and EGCG through MPN formation. The composite hydrogels were formed by incorporating mMFs into gelapin hydrogels. The mMFs significantly enhanced the mechanical properties of the hydrogel and demonstrated good biocompatibility. The possibility of tumor ablation through photothermal therapy was demonstrated in an in vivo mouse tumor model, as evidenced by reduced tumor size and disruption of tissue following hyperthermia. The potential of G-mMFs to scavenge ROS and their protective effect against oxidative stress were assessed through H_2O_2 treatment, which demonstrated a reduction in apoptosis in the presence of mMFs. The osteoinductivity of G-mMFs was shown in the form of elevated levels of expression of osteogenic markers, such as *OPN* and *OCN*, in hADSCs. The signaling pathway of osteogenesis via G-mMFs was demonstrated using an adenosine receptor agonist, and the restoration of osteogenesis in hADSCs subjected to oxidative stress was demonstrated through H_2O_2 treatment. In vivo regeneration of bone tissue was assessed using a mouse critical-bone-defect model, which produced enhanced and mature bone tissue formation in the G-mMF implanted groups. Collectively, we anticipate that this novel and multifunctional composite hydrogel, which can achieve both tumor ablation and subsequent bone-tissue regeneration, will enable a more comprehensive approach to osteosarcoma therapy.

4. Experimental Section

Materials: Poly-L-lactic acid (PLLA) was purchased from Samyang (Jeollabuk-do, Korea). 1,1,1,3,3,3-Hexafluoro-2-propanol (HFIP), 4% paraformaldehyde (PFA), and genipin were obtained from FUJIFILM Wako Pure Chemical (Osaka, Japan). Iron oxide nanopowder (Fe_3O_4, 20–30 nm, SSA: 40–60m^2 g^{-1}, Morphology: spherical) was obtained from US Research Nanomaterials (Houston, TX, USA). Isopropanol, ethylenediamine, potassium chloride (KCl), sodium phosphate (Na_2HPO_4), sodium bicarbonate ($NaHCO_3$), EGCG, gelatin, collagenase, Alizarin red S, Tween-20, ortho-phenanthroline, iron chloride ($FeCl_3$), ascorbic acid, 3% hydrogen peroxide, and biotin anti-rabbit immunoglobin G (IgG) were sourced from Sigma Aldrich (St. Louis, MO, USA). Calcium chloride ($CaCl_2$) was obtained from Duksan (Kyunki-do, Korea). Sodium chloride (NaCl) and magnesium chloride ($MgCl_2$) were purchased from Junsei (Tokyo, Japan). Live/dead assay kits and Alexa Fluor 488 Phalloidin were sourced from Invitrogen (Carlsbad, CA, USA). Fetal bovine serum (FBS), Dulbecco's phosphate-buffered saline (DPBS), penicillin-streptomycin (P/S), and trypsin/EDTA (TE) were purchased from Wisent (St. Bruno, QC, Canada). A QuantiChrom calcium assay kit was purchased from Bioassay Systems (Hayward, CA, USA), and PSB-603 was purchased from Tocris (Bristol, England). Frozen section compound (FSC) was obtained from Leica Biosystems (Richmond, VA, USA). Basal media and hADSCs were obtained from CEFOBIO (Seoul, Korea). 4′,6-Diamidino-2-phenylindole (DAPI) mounting solution was ordered from Vector Laboratories Inc. (Burlingame, CA, USA), and streptavidin-FITC was obtained from Ebioscience (San Diego, CA, USA). Primary antibodies of anti-RUNX2, OPN, and OCN were obtained from Abcam (Cambridge, MA, USA). Harris hematoxylin and Eosin Y alcohol were sourced from BBC Biochemical (Mount Vernon, MA, USA). The components of real-time quantitative polymerase chain reaction (RT-qPCR), including an RNeasy Mini Kit, Maxime RT Premix, and SYBR Premix Ex-Taq, were purchased from Qiagen (Valencia, CA, USA), Intron (Seoul, Korea), and Takara Bio (Otsu, Japan), respectively.

Preparation of Magnetic Fibers: MFs were prepared by electrospinning a PLLA solution dispersed with MNPs. Briefly, 2% of MNPs in HFIP dispersed using a sonicator (BRANSON, St. Louis, MO, USA) were mixed with an equal volume of a 6% PLLA solution. The PLLA solution, mixed with MNPs, was ejected into a rotating collector (1,000 rpm) at 2 mL h^{-1} via a syringe pump (KD Scientific, PA, USA) to fabricate aligned magnetic nanofiber sheets. Sheets were dried overnight in a vacuum desiccator, embedded in an FSC, and sectioned at 100 µm length using a Cryostat microtome (Leica biosystems GmbH, Wetzlar, Germany). The sectioned fibers were washed three times with 70% ethanol and sonicated for 3 min. Sectioned nanofiber sheets were washed with 70% ethanol five times and sonicated for 3 min. The fibers were incubated with 10% ethylenediamine solution for 1 h at room temperature with mild shaking and lyophilized for further use.

Fabrication of mMFs: The mMFs were synthesized through self-assembly of EGCG with mineral ions in a high-phosphate 10× SBF solution (HP-SBF: 58.43 g NaCl, 0.3538 g KCl, 3.6754 g $CaCl_2$, 1.016 g $MgCl_2$, and 2.8 g Na_2HPO_4 in 1 L of distilled water (DW), pH 4.35). MFs were submerged in 3 mg mL^{-1} HP-SBF and allowed to react for 60 min at 37 °C with 1 mg mL^{-1} EGCG and 0.02 M $NaHCO_3$. The MFs were then exposed to 200 µL of 1N NaOH at room temperature for 10 min, rinsed with deionized water, and lyophilized for future application. The surface morphology of the resulting fibers was examined using a field-emission scanning electron microscope (FE-SEM; JSM 7600F, JEOL, Tokyo, Japan) and XPS

(ESCALAB 250Xi, Thermo Fisher Scientific, Waltham, UK). MNPs within the fibers were examined using high-resolution TEM (JEM-3010, JEOL, Tokyo, Japan). The surface chemistry of the mMFs was examined using FTIR (Nicolet 6700, Thermo Fisher Scientific, Waltham, UK). The ROS-scavenging ability of fibers was evaluated by allowing them to reaction with an O-phenanthroline solution (1 mg mL^{-1} orthophenanthroline plus 1 mM $FeCl_3$ in distilled water), with the iron conversion rate standardized against ascorbic acid. For quantitative analysis of total phenol content, the fibers were dispersed in deionized water using a sonicator, allowed to react with 200 µL of Folin-Ciocalteu reagent for 10 min, and then incubated with 600 µL of 2% sodium carbonate for 1 h at room temperature. Absorbance was measured at 760 nm using a microplate reader. A QuantiChrom calcium assay kit (BioAssay Systems, Hayward, CA, USA) was used to assess the calcium contents on the fibers. The fibers were submerged in a 0.6 N HCl solution overnight at 37°C and subsequently allowed to react with the calcium assay reagent for 3 min, after which absorbance was recorded at 612 nm.

Fabrication of Hydrogels Incorporating mMFs (G-mMFs): Different concentrations of mMFs (0, 2, and 4 mg mL^{-1}) were mixed with a 10% genipin solution (w/w) and a 10% gelatin solution (w/v). Four milliliters of the gelatin-genipin solution were injected into a bespoke PTFE mold, frozen at −18°C for 2 h, and lyophilized overnight. The hydrogels were hydrated in water and punched into a circular form 8 mm in diameter. The storage modulus of each hydrogel was assessed utilizing a rheometer (HR10, TA Instruments; New Castle, DE, USA) under an axial force of 0.4 N and a strain of 1%. The weight of the samples was measured prior to and subsequent to lyophilization to determine the swelling ratio:

$$Swelling\ ratio = \frac{Wet\ weight - Dry\ weight}{Dry\ weight} \quad (1)$$

The Ca/P and Fe ratios were assessed using EDS (Aztec, Oxford Instruments, Oxford, UK), while the internal structure of G-mMFs was examined via FE-SEM. For Von Kossa staining, the specimens were immersed in a 2% silver nitrate solution and subjected to 60 W of illumination, followed by immersion in 5% sodium thiosulfate. The stained specimens were examined using an optical microscope. The mass loss of the hydrogels was assessed under both non-enzymatic and enzymatic experimental conditions. The hydrogels underwent non-enzymatic degradation analysis by being incubated in PBS for 8 weeks at 37 °C. The hydrogels underwent enzymatic degradation by being treated with a collagenase solution (1.0 CDU mL^{-1} collagenase diluted in PBS) and incubated for 4 h at 37 °C. The hydrogel weights were recorded at each time point. The Fe conversion assay, Folin-Ciocalteu assay, and calcium quantification were conducted as described above.

The hADSCs with a passage number less than 7 were cultured under standard conditions (37 °C and 5% CO_2) using basal media supplemented with 10% FBS and 0.5% P/S. The cells were inoculated onto sterilized hydrogels containing varying concentrations (0, 2, and 4 mg mL^{-1}) of mMFs at a density of 1×10^4 cells per gel. Live/dead staining was conducted utilizing calcein AM (1:1000) and ethidium bromide (1:2000) in the culture media. Following a 10 min incubation period, the cells were examined with a fluorescence microscope (TE 2000; Nikon, Tokyo, Japan). The DNA content of the cell-cultured hydrogels was quantified using a Quant-iT PicoGreen dsDNA Assay Kit (Invitrogen, Carlsbad, USA) in accordance with the manufacturer's instructions. Fluorescence intensity was quantified with a microplate reader (Varioskan LUX, Thermo Scientific, Waltham, MA, USA).

Photothermal Effect of G-mMFs: Photothermal images of G-mMFs were acquired using a GTC 400C (Bosch, Germany) with laser irradiation by an FC-808-10W apparatus (Changchun New Industries Optoelectronics Tech. Co, CNI, China). The stability of the photothermal effect was evaluated by monitoring temperature variations during NIR activation cycles. To assess the photothermic impact of the hydrogels on cancer cells, MG63 cells were cultured with G-mMFs (0, 4, and 8 mg mL^{-1}) and exposed to NIR laser irradiation (808 nm, 1.5 W cm^{-2}) for 3 min. Cell viability was evaluated using the live/dead assay and a DNA assay as previously described. The release of calcium and EGCG from hydrogels was quantified using a supernatant of G-mMFs (0, 4, 8 mg mL^{-1}) in DW over 72 h.

In vivo, experiments assessing temperature variations in G-mMFs during NIR irradiation were performed on 6-week-old female NOD SCID mice to confirm the thermal generation effect of G-mMFs within the organism. G-mMFs with different concentrations of mMFs were implanted subcutaneously in mice and compared with control mice that did not receive G-mMF implants. The temperature variations at the implantation site were monitored during NIR irradiation using a thermal imaging camera (GTC-400C, BOSCH, Germany). To validate the photothermal inhibition of osteosarcoma growth by G-mMFs, an in vivo experiment was performed using a xenograft mouse model. Initially, 6×10^6 Saos-2 osteosarcoma cells were suspended in 300 µL of Matrigel and injected subcutaneously into the dorsal region of NOD SCID mice (6 weeks old, female). When the tumor volume reached ≈200 mm^3, the mice were randomly assigned to the following groups: control, control + NIR, 0 mg mL^{-1}, 0 mg mL^{-1} + NIR, 8 mg mL^{-1}, and 8 mg mL^{-1} + NIR ($n = 4$). The + NIR groups were exposed to NIR irradiation. All groups, excluding the control and control + NIR, underwent surgical incision of the skin adjacent to the tumor site, followed by direct implantation of G-mMFs above the tumor. Subsequent to the implantation of the G-mMFs, the incision was sutured. The NIR-treated groups received NIR irradiation at the tumor site at an intensity of 1.5 W cm^{-2} for 5 min every 2 days for 14 days. During the experiment, mouse weight was recorded every two days, and tumor dimensions including length (L), width (W), and height (H) were assessed with a vernier caliper. The tumor volume was calculated using the following equation:

$$Tumor\ volume = 0.52 \times L \times W \times H\ (mm^3) \quad (2)$$

Upon completion of the experiment, the mice were euthanized, and the tumors were excised. Tumors from all groups were preserved in 4% PFA solution for 24 h. Thereafter, the extent of tumor growth inhibition was assessed by quantifying the mass of the excised tumors. The paraffin sections of the fixed tumors were stained using an H&E staining kit (ab245880, Abcam, England) following the manufacturer's instructions. The animals were handled in compliance with guidelines sanctioned by the Institutional Animal Care and Use Committee of DGIST (DGIST-IACUC-24010209-0002).

Cytotoxicity and ROS Scavenging Activity of G-mMFs: To evaluate the cytotoxicity of ROS, varying concentrations of H_2O_2 were administered to hADSCs cultured on hydrogels. Live/dead staining was conducted following a 24 h treatment with 1000 µM H_2O_2, as previously described. DNA content was quantified following 24 h of incubation with 500 and 1000 µM H_2O_2. Apoptosis of hADSCs on the hydrogels was assessed using the TUNEL assay. hADSCs on the hydrogels were fixed with 4% PFA following 24 h of treatment with 500 µM H_2O_2. Subsequently, apoptosis was detected using the ApopTag Fluorescein in Situ Apoptosis Detection Kit (Millipore, CA, USA) in accordance with the manufacturer's guidelines, and the samples were examined using a fluorescence microscope. TUNEL-positive cells were analyzed using the following equation:

$$TUNEL\ positive\ cells = \frac{Number\ of\ TUNEL\ positive\ nuclei}{Total\ number\ of\ nuclei} \times 100(\%) \quad (3)$$

Genes associated with apoptosis and antioxidation were examined following cell lysis in RLT buffer to extract mRNA after a 24 h culture in 500 µM H_2O_2. mRNA was isolated using the RNeasy Mini Kit (Qiagen, Valencia, USA), and cDNA was synthesized with Maxime RT Premix (iNTRON Biotechnology, Gyeonggi-do, Korea). RT-qPCR was conducted using a StepOnePlus thermocycler (Applied Biosystems, Foster City, USA) for amplification over 40 cycles, involving a melting phase at 95 °C for 15 s, an extension phase at 60 °C for 50 s, and a melting curve stage from 60 °C to 95 °C at 0.5 °C increments every 5 s. Comparative threshold cycle (Ct) values were used in analyses and normalized to *glyceraldehyde-3-phosphate dehydrogenase* (*GAPDH*) expression. The primer sequences were: *GAPDH* (Fw: 5′-CAA GGC TGT GGG CAA GGT-3′, Rv: 5′- GGA AGG

CCA TGC CAG TGA-3′); *BCL-XL* (Fw: 5′-CTG AAT CGG AGA TGG AGA CC-3′, Rv: 5′-TGG GAT GTC AGG TCA CTG AA-3′); *BCL-2* (Fw: 5'-GAG GAT TGT GGC CTT CTT TG-3', Rv: 5'-ACA GTT CCA CAA AGG CAT CC-3'); *BAX* (Fw: 5'-TTT GCT TCA GGG TTT CAT CC-3', Rv: 5'-CAG TTG AAG TTG CCG TCA GA-3'); *CAS3* (Fw: 5'-TTT TTC AGA GGG GAT CGT TG-3', Rv: 5'-CAG TGT TCT CCA TGG ATA CC-3'); *CAS9* (Fw: 5'-ATG GAC GAA GCG GAT CGG -3', Rv: 5'-TTA TGA TGT TTT AAA GAA AAG TT-3'); *CAT* (Fw: 5'-GCC TGG GAC CCA ATT ATC TT-3', Rv: 5'-GAA TCT CCG CAC TTC TTC AG-3').

Osteogenic Differentiation of hADSCs on G-mMFs: The hADSCs were cultured on G-mMFs for 14 days in growth media to evaluate osteogenic differentiation. Expression of osteogenic markers was assessed through immunofluorescent staining using OPN and OCN antibodies. Hydrogels containing hADSCs were hydrated and incubated overnight at 4 °C with anti-OCN and anti-OPN antibodies diluted 1:100 in a blocking buffer composed of 5% FBS and 0.1% Tween-20 in PBS. Thereafter, samples were incubated with anti-mouse IgG biotin-conjugated secondary antibodies (1:100 dilution in blocking buffer) and FITC-conjugated streptavidin antibodies (1:100 dilution in blocking buffer) for 1 h at 37 °C. The hydrogels were subsequently affixed with DAPI-containing mounting media and examined using fluorescence microscopy. For the ALP assay, cells cultured for 7 days on the hydrogels were lysed with RIPA buffer and incubated with p-nitrophenyl phosphate solution at 37°C for 30 min. The absorbance of the solutions was measured following treatment with a 3N NaOH assay normalized against the DNA content at each time point. The variation in calcium assay results from day 0 to day 14 was used to evaluate the increase in calcium, employing the calcium assay. A working solution of 2% Alizarin red S was used to visualize calcium deposition in the cells, and the absorbance of extracted Alizarin red S was quantified at 550 nm. RT-qPCR amplification was conducted to identify the osteogenic differentiation of stem cells on G-mMFs. To evaluate adenosine signaling–mediated osteogenic differentiation, hADSCs were cultured on G-mMFs with PSB603, an A2B receptor antagonist, for 14 days. Stem cells were cultured with or without 200 µM H_2O_2 to evaluate their osteogenic capacity under ROS conditions. RT-qPCR was conducted to evaluate the expression of osteogenic markers utilizing the designated primer sequences. *OPN* (Fw: 5′-TGA AAC GAG TCA GCT GGA TG-3′, Rv: 5′-TGA AAT TCA TGG CTG TGG AA-3′); *OCN* (Fw: 5′-GTG CAG AGT CCA GCA AAG GT-3′, Rv: 5′-TCA GCC AAC TCG TCA CAG TC-3′)

Analysis of In Vivo Bone Tissue Regeneration Using a Mouse Calvarial Defect Model: Hydrogels containing varying quantities of mMFs (0, 4, 8 mg mL^{-1}) were fabricated in a circular form with a diameter of 4 mm prior to implantation. To create a calvarial bone defect, 6-week-old female ICR mice were anesthetized with Zoletin (60 mg kg^{-1}) and Rompun (20 mg kg^{-1}) through intraperitoneal injection. Approval for animal experiments was secured from the Institutional Animal Care and Use Committee (IACUC) of Hanyang University (2022-0246A). Subsequently, calvarial defects 4 mm in diameter were established using a surgical trephine drill, and the hydrogels were inserted into the defects. After 8 weeks, the mice were euthanized via CO_2 asphyxiation, and the calvarial bones were harvested. The bones were fixed in 10% formalin for 3 days and examined using microcomputed tomography (mCT; Skyscan 1176, Billerica, MA, USA). The images were reconstructed using 3D viewer software. Analysis of regenerated bone volume (BV) to total volume (TV) was conducted utilizing CTAn and CTvol software. Adobe Photoshop (Adobe Systems) was used to compute the regenerated bone area. The samples were subsequently immersed in Rapidcal for 7 days for decalcification and then embedded in a paraffin block to produce section slices 5 µm thick. The sectioned samples were deparaffinized and subjected to hematoxylin treatment for 10 min and stained for 8 min with eosin Y solution. Goldner's trichrome staining was performed with 10 min with hematoxylin, 30 s with ponceau, 5 min with orange G, and 6 min with light green stain, following the manufacturer's guidelines. The specimens stained with H&E and Goldner's trichrome were examined using an optical microscope. Immunofluorescence staining was conducted on deparaffinized sections using anti-RUNX2, OPN, and OCN antibodies, following the previously described protocol. The stained samples were examined with a fluorescent microscope.

Statistical Analysis:

1) Pre-processing of data:
   a) Figures 2g and 3h: Fe conversion percentages were normalized to the value obtained using ascorbic acid as a control.
   b) Figure 3f,g: The mass loss was normalized to the initial weight measured on day 0.
   c) Figure 4i: Tumor volumes were normalized to individual body weights measured at each time point.
   d) Figure 5b: Cell viability was presented relative to the control group which was cultured without H_2O_2.
   e) Figure 5c: The percentage of TUNEL-positive cells was calculated based on the total DAPI signal in the region of interest.
   f) Figures 5d–f and 6e,f: Fold changes in mRNA expression were normalized to the expression of *GAPDH*.
   g) Figure 7b: The regenerated bone area was calculated as the proportion of the total circular defect corresponding to the orange-highlighted area in Figure 7a.
   h) Figure 7c: Volume measurements were performed using CTAn software and expressed as the percentage of regenerated hard tissue volume relative to the total defect volume.
2) Data presentation: All errors are given as standard deviation of the mean (mean ± SD).
3) Sample size:
   a) Figure 2e: $n = 6$, Figure 2f: $n = 4$, Figure 2g: $n = 4$
   b) Figure 3c: $n = 4$, Figure 3f,g: $n = 5$, Figure 3h: $n = 4$, Figure 3j: $n = 3$
   c) Figure 4c,e: $n = 3$, Figure 4h,i: $n = 4$
   d) Figure 5b,c,f: $n = 4$
   e) Figure 6b: $n = 5$, Figure 6c,e: $n = 3$, Figure 6f: $n = 4$
4) Statistical methods: Statistical significance was evaluated using unpaired Student's t-test and one-way analysis of variance (ANOVA), followed by post hoc analysis with Tukey's honestly significant difference test.
5) Software: All statistical analysis were conducted using GraphPad Prism 7 software (La Jolla, CA, USA).

Ethics Approval Statement: Approval for animal experiments was secured from the Institutional Animal Care and Use Committee (IACUC) of Hanyang University (2022-0246A) and DGIST (DGIST-IACUC-24010209-0002).

Supporting Information

Supporting Information is available from the Wiley Online Library or from the author.

Acknowledgements

H. B., T. H., and H. L. contributed equally to this work. This work was supported by the National Research Foundation of Korea (NRF) grant funded by the Korean government (MSIT) (grant no. RS- 2023–00207983 and NRF- 2021R1A2C3007817).

Conflict of Interest

The authors declare no conflict of interest.

Data Availability Statement

The data that support the findings of this study are available from the corresponding author upon reasonable request.

Keywords

bone tissue regeneration, cancer therapy, multifunctional hydrogel, photothermal therapy, reactive oxygen species

Received: May 14, 2025
Revised: June 17, 2025
Published online: June 30, 2025

[1] H. C. Beird, S. S. Bielack, A. M. Flanagan, J. Gill, D. Heymann, K. A. Janeway, J. A. Livingston, R. D. Roberts, S. J. Strauss, R. Gorlick, *Nat. Rev. Dis. Primers* **2022**, *8*, 1.
[2] C. A. Klein, T. J. F. Blankenstein, O. Schmidt-Kittler, M. Petronio, B. Polzer, N. H. Stoecklein, G. Riethmüller, *Lancet* **2002**, *360*, 683.
[3] Y. P. Liu, C. C. Zheng, Y. N. Huang, M. L. He, W. W. Xu, B. Li, *MedComm* **2021**, *2*, 315.
[4] P. Lafforgue, *Jt., Bone, Spine* **2006**, *73*, 500.
[5] X. Li, J. F. Lovell, J. Yoon, X. Chen, *Nat. Rev. Clin. Oncol.* **2020**, *17*, 657.
[6] P. Rai, S. Mallidi, X. Zheng, R. Rahmanzadeh, Y. Mir, S. Elrington, A. Khurshid, T. Hasan, *Adv. Drug Delivery Rev.* **2010**, *62*, 1094.
[7] C. Multari, M. Miola, F. Laviano, R. Gerbaldo, G. Pezzotti, D. Debellis, E. Verné, *Nanotechnology* **2019**, *30*, 255705.
[8] B. Tan, L. Huang, Y. Wu, J. Liao, *J. Biomed. Mater. Res., Part A* **2021**, *109*, 404.
[9] G. L. Koons, M. Diba, A. G. Mikos, *Nat. Rev. Mater.* **2020**, *5*, 584.
[10] R. Z. LeGeros, *Chem. Rev.* **2008**, *108*, 4742.
[11] N. Reznikov, J. A. M. Steele, P. Fratzl, M. M. Stevens, *Nat. Rev. Mater.* **2016**, *1*, 1.
[12] E. O'Neill, G. Awale, L. Daneshmandi, O. Umerah, K. W. H. Lo, *Drug Discovery Today* **2018**, *23*, 879.
[13] Y. R. V. Shih, Y. Hwang, A. Phadke, H. Kang, N. S. Hwang, E. J. Caro, S. Nguyen, M. Siu, E. A. Theodorakis, N. C. Gianneschi, K. S. Vecchio, S. Chien, O. K. Lee, S. Varghese, *Proc. Natl. Acad. Sci. USA* **2014**, *111*, 990.
[14] H. Byun, G. N. Jang, J. Lee, M.-H. Hong, H. Shin, H. Shin, *Biofabrication* **2021**, *13*, 034101.
[15] C. Dunnill, T. Patton, J. Brennan, J. Barrett, M. Dryden, J. Cooke, D. Leaper, N. T. Georgopoulos, *Int. Wound J.* **2017**, *14*, 89.
[16] H. Tao, G. Ge, X. Liang, W. Zhang, H. Sun, M. Li, D. Geng, *Acta Biochim. Biophys. Sin.* **2020**, *52*, 1055.
[17] A. Marques-Carvalho, H. N. Kim, M. Almeida, *Bone Rep.* **2023**, *19*, 101664.
[18] J. Liu, X. Han, T. Zhang, K. Tian, Z. Li, F. Luo, *J. Hematol. Oncol.* **2023**, *16*, 1.
[19] T. S. Sileika, D. G. Barrett, R. Zhang, K. H. A. Lau, P. B. Messersmith, *Angew. Chem., Int. Ed.* **2013**, *52*, 10766.
[20] N. R. Perron, J. L. Brumaghim, *Cell Biochem. Biophys.* **2009**, *53*, 75.
[21] X. Gao, Q. Wang, L. Ren, P. Gong, M. He, W. Tian, W. Zhao, *Chem. Eng. J.* **2021**, *426*, 131825.
[22] S. Lee, J. Lee, H. Byun, S. Jeong Kim, J. Joo, H. H. Park, H. Shin, *Acta Biomater.* **2021**, *124*, 166.
[23] Q. Dai, H. Geng, Q. Yu, J. Hao, J. Cui, *Theranostics* **2019**, *9*, 3170.
[24] H. S. Kim, M. J. Quon, J. A. Kim, *Redox Biol.* **2014**, *2*, 187.
[25] K. S. Ogueri, C. T. Laurencin, *ACS Nano* **2020**, *14*, 9347.
[26] J. C. Rose, M. Cámara-Torres, K. Rahimi, J. Köhler, M. Möller, L. De Laporte, *Nano Lett.* **2017**, *17*, 3782.
[27] A. Omidinia-Anarkoli, S. Boesveld, U. Tuvshindorj, J. C. Rose, T. Haraszti, L. De Laporte, *Small* **2017**, *13*, 1702207.
[28] H. Byun, S. Lee, H. Shin, *Biofabrication* **2024**, *16*, 025006.
[29] K. Dettlaff, M. Stawny, M. Ogrodowczyk, A. Jelińska, W. Bednarski, D. Wątróbska-Świetlikowska, R. W. Keck, O. A. Khan, I. H. Mostafa, J. Jankun, *Int. J. Mol. Med.* **2017**, *40*, 329.
[30] H. Byun, G. N. Jang, H. Jeong, J. Lee, S. J. Huh, S. Lee, E. Kim, H. Shin, *Biomater. Res.* **2023**, *27*, s40824.
[31] J. Zhang, H. Sato, H. Tsuji, I. Noda, Y. Ozaki, *Macromolecules* **2005**, *38*, 1822.
[32] H. Jeong, H. Byun, J. Lee, Y. Han, S. J. Huh, H. Shin, *Adv. Healthcare Mater.* **2024**, *1*, 2400232.
[33] H. Byun, G. N. Jang, M. H. Hong, J. Yeo, H. Shin, W. J. Kim, H. Shin, *Nano Convergence* **2022**, *9*, 47.
[34] Y. Yu, S. Xu, S. Li, H. Pan, *Biomater. Sci.* **2021**, *9*, 1583.
[35] S. Utech, A. R. Boccaccini, *J. Mater. Sci.* **2015**, *51*, 271.
[36] N. Kashimura, Y. Suzuki, T. Nonoyama, J. P. Gong, *Chem. Mater.* **2024**, *36*, 2944.
[37] Y. Huang, X. Li, Z. Lu, H. Zhang, J. Huang, K. Yan, D. Wang, *J. Mater. Chem. B* **2020**, *8*, 9794.
[38] Z. Pan, L. Brassart, *J. Mech. Phys. Solids* **2022**, *167*, 105016.
[39] M. I. Wahba, *Polym. Bull.* **2024**, *81*, 14251.
[40] G. M. Cooper, *The Cell. 2nd ed*, Sinauer Associates, Sunderland, MA, **2000**, 1394–403.
[41] H. Fujiki, T. Watanabe, E. Sueoka, A. Rawangkan, M. Suganuma, *Mol. Cells* **2018**, *41*, 73.
[42] J. H. Lim, D. E. Kim, E. J. Kim, C. D. Ahrberg, B. G. Chung, *Macromol. Res.* **2018**, *26*, 557.
[43] M. Overchuk, R. A. Weersink, B. C. Wilson, G. Zheng, *ACS Nano* **2023**, *17*, 7979.
[44] I. B. Slimen, T. Najar, A. Ghram, H. Dabbebi, M. Ben Mrad, M. Abdrabbah, *Int. J. Hyperthermia* **2014**, *30*, 513.
[45] Y. Yao, H. Zhang, Z. Wang, J. Ding, S. Wang, B. Huang, S. Ke, C. Gao, *J. Mater. Chem. B* **2019**, *7*, 5019.
[46] A. Lewinska, M. Wnuk, E. Slota, G. Bartosz, *Clin. Exp. Pharmacol. Physiol.* **2007**, *34*, 781.
[47] X. Gao, Z. Xu, G. Liu, J. Wu, *Acta Biomater.* **2021**, *119*, 57.
[48] R. Kanlaya, S. Khamchun, C. Kapincharanon, V. Thongboonkerd, *Sci. Rep.* **2016**, *6*, 30233.
[49] J. Jeong, J. H. Kim, J. H. Shim, N. S. Hwang, C. Y. Heo, *Biomater. Res.* **2019**, *23*, 4.
[50] S. Y. Shin, C. G. Kim, E. H. Jho, M. S. Rho, Y. S. Kim, Y. H. Kim, Y. H. Lee, *Cancer Lett.* **2004**, *212*, 225.
[51] D. Wang, Y. Wang, S. Xu, F. Wang, B. Wang, K. Han, D. Sun, L. Li, *Stem Cells Int.* **2016**, *2016*, 7532798.
[52] M. L. Zoch, T. L. Clemens, R. C. Riddle, *Bone* **2016**, *82*, 42.
[53] W. Wang, K. W. K. Yeung, *Bioact. Mater.* **2017**, *2*, 224.

